

Electrospray Deposition, Model, and Experiment: Toward General Control of Film Morphology

Ivo B. Rietveld,^{*,†} Kei Kobayashi,[‡] Hirofumi Yamada,[†] and Kazumi Matsushige[†]

Department of Electronic Science and Engineering, Kyoto University, Katsura A1-326, Nishikyo-ku, Kyoto 615-8510, Japan, and International Innovation Center, Kyoto University, Katsura, Nishikyo-ku, Kyoto 615-8520, Japan

Received: July 3, 2006; In Final Form: August 27, 2006

Poly(vinylidene fluoride) film formation with electrospray deposition has been studied with support of a droplet evaporation model. The input parameters of the model consist basically of the solvent, the solute concentration, the flow rate, and the solution conductivity. The model provides the droplet size, the solute concentration, the droplet velocity, and the shear stress of the droplet at impact as a function of the distance between the nozzle and the substrate. With some additional experimental information such as the size change of the film with spray distance and the viscosity of the solution, the growth rate of the film and the shear rate of the droplet at impact can be determined. Growth rate is shown to define distinct regimes of film formation. In those regimes, only a single factor or a limited number of factors controls the film morphology. The most important factors include the shear rate and the surface energy. It is found that at a specific range of growth rates only the shear rate determines the morphology of the polymer film. Growth rate, as the defining quantity of film morphology, is not limited to polymer solutions. Therefore, the growth rate, in combination with the control factors mentioned above, functions as a general framework through which understanding and control of film formation with electrospray deposition can be improved.

1. Introduction

Electrospray or electro-hydrodynamic atomization is becoming more and more popular for the preparation of nanoparticles, thin polymeric fibers, and thin films. Interest in the electrospray process grew after its application in electrospray mass spectrometry.^{1,2} In the early 1990s different spraying modes and their stability were investigated experimentally by Cloupeau et al. and others.^{3–5} A decade ago, most of the attention was aimed at the theoretical description of the monodisperse droplet size and controlled production of particles.^{6–9} These monodisperse particles can be used for example for dispensing precise quantities of medicine into the lungs.¹⁰ Interest spread into electrospinning, the production of polymer fibers with electrospray,¹¹ and into thin film production. Thin film production with electrospray can be divided into two areas: inorganic^{12,13} and organic, with an emphasis on polymeric, films.^{14–18} In the case of inorganic films spray pyrolysis is often used, a process in which the substrate is heated to 200 °C or higher.^{12,13,19} On the other hand, organic materials often cannot be processed at such high temperatures and therefore need temperatures closer to or at room temperature. Furthermore, solutions of organic compounds, in particular polymers, can have a wide range of viscosity values, which is known to have an effect on the film morphology.¹⁶ Despite recent publications of studies of polymer films produced with electrospray^{16,18,20} and of controlled deposition,²¹ a general understanding of polymer film formation with electrospray is still lacking. It is therefore important to study electrospray deposition of polymers, not the least to explain the role of viscosity in the film formation process.

A comprehensive understanding of the film formation process with electrospray deposition is not easily achieved, mainly because many factors have an influence on the resulting film. To obtain insight into the relevant factors, one can divide the electrospray deposition process into four subprocesses. The approach will be based on electrospray in the cone–jet mode, because this mode is stable and controllable.²² Now the subprocesses become (1) the cone–jet system and the factors that control its stability, (2) jet break-up and the resulting droplet size, (3) droplet evolution, and (4) deposition and film formation.

In Table 1, an overview is given of the parameters for each subprocess. For subprocess 1, cone stability, in depth discussion about the relevant factors can be found in refs 3, 5, 6, 8, and 23–25. Nozzle properties are discussed for example in refs 4 and 22. The spray geometry does not only consist of the nozzle and the spray distance; however, most of the remaining effects of the spray geometry can be included in the electric field instead. The effect of coaxial gas flow is discussed in ref 26. Factors affecting subprocess 2, the droplet size in the jet break-up, are discussed in refs 6, 7, and 9. In subprocess 2, the role of the viscosity is not completely clear yet, but it appears to be small.⁹ Most of the factors affecting subprocess 3, reduction of the droplet size, are related to droplet evaporation.²⁷ The droplet charge, however, can cause discharges if the Rayleigh limit is reached,²⁸ which often includes a reduction of the droplet size. The droplet velocity, due to the combination of the droplet size and charge and the electric field, determines in part how much time the droplet has available for evaporation, before impact on the substrate occurs. The coaxial gas flow can accelerate the droplet velocity²⁹ and affect the rate of evaporation by changing the background vapor pressure of the solvent,²⁶ but coaxial gas flow will not be considered further in this paper, because in principle it can be considered secondary to other

* Corresponding author. E-mail: rietveld@piezo.kuee.kyoto-u.ac.jp.

[†] Department of Electronic Science and Engineering.

[‡] International Innovation Center.

example, the initial solution is the solution fed to the cone–jet system; the initial droplet size is the droplet size at the formation from the jet.

The spectrum of PVDF film morphologies is analyzed with support of the model, and it is shown that film morphologies are the result of relatively few parameters; these include the growth rate, the shear rate of the droplet, and the surface energy. The results presented in this paper are valid for polymer film formation with electrospray; however, electrospray deposition of other compounds will certainly benefit from the understanding provided by this analysis.

2. Theory

In this section, a model will be presented, which provides droplet properties at impact as a function of the electrospray process parameters, introduced above. Only the cone–jet mode is considered with a monodisperse droplet size distribution. In reality, electrospray often produces bimodal distributions, due to small satellite droplets that form during the breakup of the main droplets.⁹ It is assumed that the satellite droplets are so small that they have a negligible effect on the film formation and other process parameters. Furthermore, it is assumed that the jet has a flat velocity profile and varicose break-up as defined in refs 6–9. Some information about the case in which the velocity profile is not flat⁷ will be given in the Appendix. In addition, the case of a whipping jet break-up in contrast to a varicose break-up⁹ will be discussed briefly.

Current Generated in the Cone–Jet. Strictly speaking, the prediction of the current is not part of the model, because in many cases it will be easier to use the measured current during the spray process. However for predictions, advance knowledge of the current may be necessary. According to Hartman et al., the current, I , for a flat velocity profile in the jet is given by⁸

$$I = a_I(KQ\sigma)^{1/2} \quad (1)$$

with a_I a proportionality constant, K conductivity, Q flow rate, and σ surface tension. Gañán-Calvo obtained a similar relationship and determined a general value for the proportionality constant.⁶ However, that relationship is more complicated and does not appear to be more precise; therefore, eq 1 is used in this paper. Despite the fact that eq 1 is only valid for a flat velocity profile, it is reasonably robust, especially if a_I is determined specifically for the solution that is sprayed. Equations for a nonflat profile are given in the Appendix.

Prediction of Droplet Size. According to Hartman et al., jet break-up in the cone–jet mode has two regimes determined by the ratio of the electric stress and the surface tension. If the electric stress is low enough, varicose jet break-up occurs. The droplet diameter, d , is in such a case determined by⁹

$$d = a_d \left(\frac{\rho \epsilon_0 Q^4}{I^2} \right)^{1/6} \quad (2)$$

with a_d a proportionality constant, ρ density of the solution (solvent), and ϵ_0 dielectric constant of vacuum. Equation 2 is independent of the velocity profile in the jet. Since it is not always clear if eq 1 applies and since all equations can deviate from the experimental current, the measured current is the preferred input parameter in eq 2. In a slightly different form, eq 2 is found in ref 6 and an estimate for a_d is also given.

Determination of Varicose/Whipping Jet Break-up. Whipping jet break-up is caused by excess electric surface stress on the jet with respect to the surface tension. If the ratio exceeds

~ 0.3 , eq 2 breaks down and the droplet size, d , has to be calculated with⁹

$$d = \left(0.8 \frac{2.88 \epsilon_0 \sigma Q^2}{I^2} \right)^{1/3} \quad (3)$$

which is derived from the Rayleigh limit. Which of the two equations, 2 or 3, is valid can be determined by calculating both radii. The smallest radius represents the valid equation and break-up mode.⁹

The distribution of the droplet size is rather narrow in the varicose jet break-up, although small satellite droplets are likely to form between the main droplets. In the whipping jet break-up more satellite droplets will form, which affects the size distribution, causing the spray to be much less defined. This will affect the droplet evolution, and since the model is based on the assumption of a single size distribution, it is better to avoid a whipping jet break-up, if one does not want to complicate the analysis.

Droplet Evaporation. Basically, the lifetime of a 1–10 μm diameter droplet can be calculated in a fairly simple way. Depending on the different conditions such as droplet size and solute, the basic calculation can be extended with correction factors. The driving force of the evaporation is the partial pressure difference between the solvent in the droplet and in the spray chamber. The temperature drop of the droplet is incorporated because this effect is generally large. Other effects, like the Kelvin effect and the Fuchs effect can be ignored for droplets down to about 1 μm .²⁷ In any case, other effects, such as background vapor pressure, solute concentration, and droplet speed and location will most likely cause larger deviations to the eventual result of this model than the Kelvin and Fuchs effects. In the case of larger droplets ($> 10 \mu\text{m}$), ref 31 gives additional correction factors not implemented in this model.

The rate of evaporation of a droplet is described by the following equation:²⁷

$$\frac{\partial d}{\partial t} = \frac{4DM}{R\rho d} \left(\frac{p_C}{T_C} - \frac{p_d}{T_d} \right) f \quad (4)$$

with t time, D diffusion of a solvent molecule in air, M molar weight of a solvent molecule, R gas constant, ρ the density of the solution in the droplet, p_C vapor pressure of the solvent in the spray chamber, T_C temperature in the chamber, p_d vapor pressure of the droplet, and T_d temperature of the droplet. The coefficient f corrects eq 4 for the presence of forced convective flow around the droplets, which is caused by the transport of the charged droplets to the substrate under the influence of an electric field; however, if the droplets are small enough or, more generally, if the Reynolds number is small enough, $f \approx 1$. It will be shown in the Appendix that, in the present case, this is an acceptable approximation. In the case of larger droplets ($> 10 \mu\text{m}$), correction factors should be taken into account.

Temperature decrease of the droplet during evaporation is dependent on the balance between the loss of energy due to evaporation and a restoring effect due to the chamber temperature:^{27,32}

$$\frac{\partial T_d}{\partial t} = \frac{1}{d} \left[\frac{3H}{C_p M} \frac{\partial d}{\partial t} + \frac{12h_{\text{air}}}{C_p \rho} (T_C - T_d) \right] \quad (5)$$

with H the heat of evaporation of the solvent, C_p heat capacity of the droplet (solvent in dilute case), and h_{air} the heat-transfer coefficient of air.

Droplet Charge. Electrospray is an electrochemical cell, and a small current travels with the droplets to the substrate. Since the droplet distribution is narrow, the charge can be assumed to be evenly distributed over the droplets. With knowledge of the current, the flow, and the droplet size, the charge per droplet can then be obtained. If a droplet evaporates, the charge will not change until the Rayleigh limit is reached; the maximum charge for a droplet q_{\max} is defined as²⁸

$$q_{\max} = \pi(8\epsilon_0\sigma d^3)^{1/2} \quad (6)$$

Once at this limit, the droplet will have to expel charge²⁸ and the remaining charge on the droplet will average around 80% of the Rayleigh limit.^{9,28} Droplets expelling charge also expel solution in the process. Generally 15% of the charge is expelled with about 2% of the solution.²⁸ This accelerates the decrease of the droplet size, but the influence on the total time of evaporation depends on the moment when the first discharge takes place. If eq 3 applies, discharge will start almost immediately after droplet generation and the total evaporation time may decrease by about 10%. If eq 2 applies, the first discharge may very well occur after the deposition of the droplet on the substrate, and in that case, it would not be important for the calculation of the droplet evolution. Employing the varicose jet break-up provides, besides the monodisperse size distribution, the additional advantage that the Rayleigh limit will be reached at a late stage in the droplet evaporation, not affecting droplet size decrease to a large extent.

The model incorporates droplet charge loss when the Rayleigh limit is reached by keeping the charge on the droplet at 80% of the Rayleigh limit. Because the simultaneous liquid loss is low, 2% per discharge, and discharge happens at a late stage of the droplet evolution in the case of varicose jet break-up, the liquid loss is not incorporated into the model. In most cases, droplets impinge before the Rayleigh limit is reached; this will be shown in Results.

Location of the Droplet. To determine the state of a droplet at deposition, the position of a droplet as a function of time has to be known. The motion of a charged droplet in the axial direction of the spray under influence of an electric field can be described with²⁹

$$\frac{\pi}{6}d^3\rho \frac{dv}{dt} = -3\pi d\mu f_d v + q\bar{E} \quad (7)$$

v is the velocity of the droplet (in relation to the medium), μ is the (dynamic) viscosity of the medium (in this paper nitrogen atmosphere), f_d is a coefficient which compensates for the effect of nonzero Reynolds number, and E is the electric field. The interactions between the charged particles have been left out of eq 7, under the assumption that they will cancel out in the axial direction.

Electrospray-generated droplets have an initial velocity, due to the liquid velocity in the jet. A simple approach to calculate the initial velocity is to match the droplet volume with the jet volume determined by the wavelength of the instability on the jet just before break-up; according to Rayleigh this wavelength is $\lambda = 4.5d_{\text{jet}}$. The assumption that the flow rate of the spray is conserved in the jet leads to the following estimate for the initial velocity of the droplet:⁵

$$v_i = \frac{Q}{(1/4)\pi(d_i/1.89)^2} \quad (8)$$

where the index “i” stands for “initial”.

In this paper the emphasis is on droplets with a diameter between 1 and 5 μm . This allows for a number of approximations. The Reynold's number will be small, and therefore the drag factor f_d can be taken as 1.³³ Furthermore, due to the small mass of the droplets the momentum of the initial velocity is quickly dominated by the balance of the electric force and the viscous drag force. Therefore, the left side of eq 7 can be taken as zero. The effect of ignoring the initial velocity and its momentum will be shown in Results. The velocity of the droplet can now be expressed as

$$v = \frac{Eq}{3\pi\mu d} \quad (9)$$

A further simplification is the approximation of the electric field by a constant value. In principle the electric field between a sharp tip and a flat surface can be calculated,^{29,31} but by introducing a ring around the tip of the nozzle, the field can be approximated with a constant field between the ring and the substrate. This is not only because the ring adds its field to the field generated by the nozzle but also because the required potential for a stable cone-jet is adjusted due to the potential of the ring in such a way that the field, generated between the nozzle and the substrate, adjusts to become roughly similar to the field generated by the ring. Although the field is very high near the tip of the nozzle, it falls off very fast too. The constant potential on the ring simplifies the calculation of the field to a linear dependence on the spray distance:

$$E = \frac{\Delta V}{s} \quad (10)$$

with ΔV the potential difference between the ring and the substrate and s the distance between the nozzle tip-ring and the substrate (Figure 1). This approach does not appear to introduce large errors in the calculation of the droplet velocity as long as the distance between the nozzle-ring and the substrate does not become too short in relation to the spray geometry. The differences between velocity calculated with eq 10 and with an electric field evaluated with a finite element method will be shown in Results.

The last approximation is the use of an average droplet size—and average charge, but charge does not change as long as the Rayleigh limit has not been reached—averaged over the droplet evolution time. In this way a vector is created containing average droplet sizes as a function of time. The aim of this model is to evaluate the state of the droplet at deposition. By combining eqs 9 and 10, multiplying with the time t belonging to each average, and taking spray distance s equal to droplet position s , one obtains

$$s = \left(\frac{\Delta V \bar{q} t}{3\pi\mu d} \right)^{1/2} \quad (11)$$

The location $s(t)$ is the location of the droplet at deposition and therefore also the position of the substrate with respect to the tip of the nozzle. A plot of s versus t should therefore not be read as a trajectory of a droplet versus t , but as the impact location of the droplet needing time t to impinge on the substrate. Equation 11 facilitates comparison of experimental films prepared as a function of spray distance with the state of the droplet calculated with the model. The velocity of the droplet at position s can be calculated with eq 9 with use of the proper $d(t)$ and $q(t)$ (not the average values).

Even though expressions exist which describe the course of an electric field between a sharp tip and a surface,^{29,31} the use

of such expressions in combination with the droplet evolution will have the disadvantage that for each spray distance the pathway has to be calculated separately, which will demand more calculation power and time. Furthermore there is a parameter within the evolution model, which cannot be determined easily: the vapor pressure of the solvent in the chamber, or better within the spray. The vapor pressure within the spray depends on the evaporation rate of the droplets but also on the diffusion of the solvent vapor out of the spray. Since calculating this value has so far not led to reliable results,³¹ the vapor pressure is most easily deduced experimentally from the spray distance where the film is/becomes dry. However since this estimate contains the spray distance instead of the time, any error in the calculation of the distance will be compensated with the experimental determination of the vapor pressure. In Results it will be shown that the differences between this approach and a more precise one are not very large; therefore, the use of a more exact approach to calculate the distance appears to be unnecessary.

Film Formation: Shear Stress and Droplet Flow. To predict the film morphology, two electrospray-controlled factors were shown to be important: the droplet size and the flow of the droplet.¹⁶ An impression of the droplet flow on the substrate can be obtained by estimating the stress, τ , on the droplet at deposition:

$$\tau = \frac{F}{A} = \frac{(1/2)mv^2}{r} \frac{1}{\pi r^2} = (2/3)\rho \frac{\pi r^3 v^2}{\pi r^3} = (2/3)\rho v^2 \quad (12)$$

F is the force resulting from the droplet impact on a surface A , approximated with the droplet size: πr^2 , with r the droplet radius. Most of the droplets used for film formation are reasonably fluid and can fully spread; therefore, the droplet momentum dissipates by approximation over distance r . The droplet center of mass is a distance r away from the substrate at impact, and after the droplet has spread over the substrate the center of mass is approximately at the substrate.

Using the definition of viscosity, an estimate of the shear rate, γ , of an impinging droplet can be obtained:

$$\gamma = \frac{\tau}{\eta} \quad (13)$$

with η the viscosity of the solution.

Model. The droplet size is determined with eqs 2 and 3; eqs 4 and 5 are solved numerically to determine the droplet radius as a function of time. The average diameter as a function of time is determined together with the initial charge on the droplet, and eq 6 is used to check if the Rayleigh limit is not exceeded. The size and charge average are used with eq 11 to replace the main variable t with s , the spray distance. As a function of s the velocity of the impinging droplet will be obtained with eq 9 using the regular q and d . Finally, the combination of eqs 12 and 13 provides an estimate of the shear rate of the droplet at deposition.

3. Experimental Methods

Materials. Poly(vinylidene fluoride) (PVDF) was purchased from Sigma Aldrich; MW, 534 000 g/mol. Saccharose and *N,N*-dimethylformamide (DMF), 99.7%, were obtained from Nacalai Tesque, Japan. Ammonium nitrate, 99.0%, was purchased from Wako Ltd., Japan. All chemicals were used as purchased. Silicon wafer was used as a substrate (resistance, 1–5 Ω cm), purchased

TABLE 2: Spray Potential of the Nozzle for Selected Spray Distances

distance (cm)	potential (kV)	distance (cm)	potential (kV)
1.1	4.7	2.5	5.4
1.8	5.2	3.2	5.5
2.2	5.3	7.0	5.8

from E&M, Japan. Wafers were all cleaned before use with acetone in an ultrasonic bath for at least 15 min.

Solutions were made by weighing the compound (PVDF or sucrose) in DMF. After an ultrasonic treatment of 30 min., the solutions were allowed to dissolve for at least one night. Solvent with increased conductivity was prepared by dissolving the appropriate amount of ammonium nitrate in DMF, and this solvent was subsequently used for the preparation of the solutions.

Spray Geometry. The spray geometry is shown in Figure 1. The distance from the nozzle to the substrate holder can be varied from 0 to 12 cm. For the experiments, distances were used ranging from 1 to 7 cm. The ring positioned at the tip of the nozzle had the same potential, 3 kV, in each experiment. To ensure a stable cone–jet mode, the potential of the nozzle had to be varied with the substrate distance and with the conductivity of the solution. In Table 2 selected potentials are given for important spray distances.

Equipment. The conductivity of the solutions was measured with a Horiba pH/conductivity meter D-54 and the Horiba conductivity cell 3551. The spray experiments took place in an in-house-constructed electrospray chamber with a heating element and a temperature control unit. The chamber was continuously flushed with a flow of 6 L/min nitrogen gas to keep the humidity level below 5% and to remove excess solvent vapor. It was ensured that the flow of nitrogen did not disturb the cone–jet spray. Spray solution was supplied to the nozzle with constant flow rate by syringe pump Model 22 of Harvard apparatus. In-house-constructed voltage units, containing Ultravolt Inc. voltage supply modules, were connected to nozzle and ring. The current from the substrate holder to ground was monitored during each spray experiment with a Keithley 6517 electrometer.

Sprayed particles and films were imaged with the JEOL SPM 4200 atomic force microscope. Imaging was done with tapping mode and low force on the cantilever (NSG10 cantilevers from NT-MDT, Russia).

Current Calibration (Equation 1). Determination of a_I (eq 1) was done by preparing solutions of ammonium nitrate in DMF and measuring the conductivity for all samples at 20 °C. Also pure DMF was used, which had a conductivity of 0.36 μ S/cm (20 °C). The temperature dependence of the conductivity in DMF (valid for all salt solutions up to 12 μ S/cm (20 °C)) from 20 to 90 °C has been determined:

$$\kappa_{\text{salt}}(T) = (-0.00094(T/^{\circ}\text{C}) + 0.3787) \left(\frac{\kappa_{20^{\circ}\text{C},\text{salt}}}{\kappa_{20^{\circ}\text{C},\text{pureDMF}}} \right) \quad (14)$$

with κ_{salt} the conductivity of a DMF–ammonium nitrate solution and T the temperature in °C. The relationship is relative to the conductivity of pure DMF at 20 °C. The proper relationship is more complicated,³⁴ but within the present range eq 14 is sufficiently precise.

Subsequently the solutions were electrosprayed and the current was monitored at different flow rates. The minimum current for a stable DMF cone–jet mode with the setup in Figure 1 was determined to be 20 nA. Also solutions containing

TABLE 3: Flow Rate (Q) or Concentration, Current (I , Measured), Droplet Diameter (d , Calculated with Equation 2), and Spray Distance of Solutions of PVDF in DMF, Sprayed at 40 °C

Q ($\mu\text{L}/\text{min}$)	concn (wt %)	I (nA)	d (μm)	nozzle—substrate distances ^a (cm)
1.2	.25	27	1.7	1, 1.1, 1.25, 1.4, 1.5, 2
2.5	.25	50	2.3	1, 1.5, 1.75, 2, 2.5
3.0	.25	21	3.4	1, 1.5, 2, 2.25, 2.5, 2.75, 3, 4, 5
4.0	.25	25	3.9	2.25, 2.5, 2.75, 3, 3.5, 4
6.0	.25	26	5.0	2.25, 2.75, 3, 3.25, 3.5, 3.75, 4, 5, 6, 7
3.0	0.050	32	3.0	1, 1.75, 2, 2.25, 2.5, 2.75, 3, 4
3.0	0.10	25	3.2	1, 1.5, 1.75, 2, 2.25, 2.5, 2.75, 3, 3.5, 4
3.0	0.25	21	3.4	1, 1.5, 2, 2.25, 2.5, 2.75, 3, 4, 5
3.0	0.50	23	3.3	1, 1.5, 1.75, 2, 2.25, 2.5, 2.75, 3, 3.25, 4, 5
3.0	1.0	25	3.2	1, 2, 2.25, 2.5, 2.75, 3, 4, 5

^a The error in the spray distance is ± 0.05 cm.

saccharose and PVDF have been used to determine a_I . The current has been determined in sprays at 20, 40, and some at 80 °C.

With eq 1, the presence of the cone-jet mode can be checked once a_I is known; therefore, for all solutions containing saccharose and PVDF the current was determined at various flow rates before the actual film or particle deposition.

Droplet Size Determination with Saccharose (Equation 2). To determine the droplet size and calibration constant a_d for eq 2, 0.1 wt % saccharose/DMF solutions were sprayed. The distance between the nozzle and the substrate holder was 6 cm and the chamber temperature 40 °C to ensure deposition of dry particles. Solutions were used with a conductivity of 0.75 $\mu\text{S}/\text{cm}$ and flow rate ranging from 3 to 7 $\mu\text{L}/\text{min}$ and with 11.4 $\mu\text{S}/\text{cm}$ from 0.5 to 4 $\mu\text{L}/\text{min}$. A few experiments were performed with a solution of 0.55 $\mu\text{S}/\text{cm}$ and flow rate of 3–6 $\mu\text{L}/\text{min}$ at 20 °C and 3 $\mu\text{L}/\text{min}$ at 40 and 80 °C. a_d was determined using the measured current during the spray.

Particle sizes were determined with AFM images of 25, 10, or 5 μm^2 , depending on the particle size. The height and surface area of the particles were measured. With the assumption that the volume of saccharose in the initial droplet can be neglected, the droplet size was calculated from the original concentration (0.1 wt %). Saccharose has been used to determine particle sizes, because it easily crystallizes and resists deformation caused by the AFM cantilever tip.

PVDF Deposition Morphology. Solutions of PVDF in DMF were prepared with various concentrations and conductivities, depending on the desired spray current indicated in Table 3. The solutions were sprayed at 40 °C at varying spray distances, given in Table 3. For each film, a 25 μm by 25 μm AFM image was taken at about 5 mm off-center, and the roughness average was determined (as defined in ref 16). Since roughness average depends on the scale of observation, only data from 25 $\mu\text{m} \times 25 \mu\text{m}$ images were compared. Roughness average is also dependent on the film thickness and tends to level off when a certain thickness has been reached.³⁵ The spray duration for which the roughness levels off was determined to be 20 min for a 0.25 wt % PVDF solution sprayed with 3 $\mu\text{L}/\text{min}$ at a distance of 3 cm. The experimental spray time was therefore chosen to be 24 min and was adjusted in accordance with flow rate, concentration, and spray distance, taking into account that with changing distance an area of different size will be covered by the spray.

Viscosity. The viscosity of four samples of PVDF in DMF, 3.6, 7.4, 11.4, and 15.7 % (v/v), was determined. The solutions were made by weighing the polymer and the DMF and slowly (~ 1 week) dissolving the polymer under continuous stirring and careful heating; $T < 70$ °C. The viscosity was measured both at 20 and 40 °C in a rotational viscometer, DynAlyser DAR-

100, with a Couette geometry (cup diameter, 2.7 cm; cylinder diameter, 2.5 cm). The viscosity was measured over the complete shear rate range of the apparatus, 0–100 s^{-1} , and an average value was determined with a linear fit at the higher end of the shear rate, typically 10–100 s^{-1} . The viscosity as a function of the concentration was fitted with a polynomial. Scaled literature data of dilute solutions of a slightly smaller PVDF polymer in DMF³⁶ were used to support the polynomial fit in the dilute region.

Calculations. The electric field was evaluated for the geometry presented in Figure 1 with the finite element method using FlexPDE 3.10a Professional (2003). This was done for various spray distances, using nozzle potentials presented in Table 2. A cylindrical coordinate system was used. The resulting electric field was used to calculate droplet velocities (eqs 7 and 8) and to compare those to the velocities resulting from the constant electric field approximation (eq 10).

The droplet evolution model was used to calculate all properties of the droplets with the input parameters as given in Tables 2 and 3. Additional calculations were performed to determine the effect of the various approximations used in the model. The code to evaluate the droplet evolution model was written in Matlab Version 7.1.0.246 (R14). Most of the constants used in the calculations can be found in the Appendix. A Matlab version of the model is available as Supporting Information.

4. Results

Current Dependence. In Figure 2 the spray current has been plotted against $(KQ\sigma)^{1/2}$. Both the conductivity and the surface tension have been adjusted with temperature. The slope for all data is 3.1, and for data sprayed at 40 °C only, it is 2.7. The latter value has been used for the verification of the presence of a cone-jet in spray experiments at 40 °C. With all variables adjusted for temperature, it is expected that the points for the different temperatures converge on one straight line. It is not clear why the slope of the current at 40 °C is lower than those at 20 and 80 °C. This may be caused by experimental error, but the consistency of the line may indicate that there is another temperature-dependent factor which has not been taken into account. Although in this paper the temperature dependence of the conductivity has been corrected, its change is small, especially between 20 and 40 °C (eq 14). It appears therefore sufficient to use the value measured at 20 °C, as long as the temperature range is not too large.

Particle Size Dependence. The droplet diameter has been determined as a function of flow and of solution conductivity by measuring, by AFM, the size of saccharose particles produced with electrospray. The inset of Figure 3 shows an example of a particle size distribution, where it can be seen that the spray produces a monodisperse distribution of particles. In Figure 3,

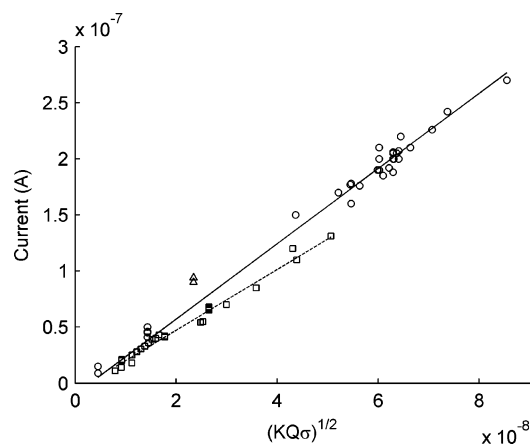


Figure 2. Current measured during spray as a function of $(KQ\sigma)^{1/2}$: open circles, spray current at 20 °C; open squares, spray current at 40 °C; open triangles, spray current at 80 °C. The solid line is a fit of all data (3.35); the broken line is the fit of 40 °C data only (2.71). The surface tension and conductivity, incorporated in the x -axis quantity, were corrected for temperature.

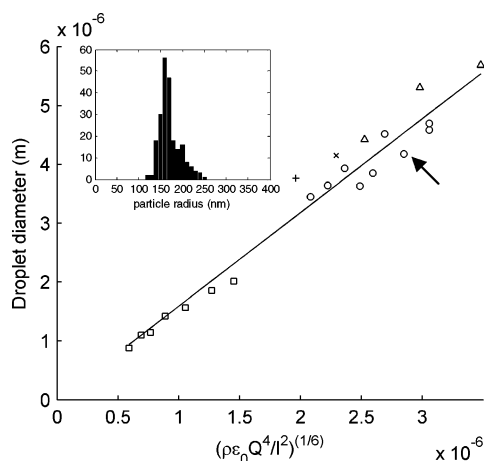


Figure 3. Droplet diameter determined with AFM versus eq 2 ($a_d = 1$) at 40 °C unless stated otherwise: open squares, droplet size for conductivity 11.4 $\mu\text{S}/\text{cm}$ and flow rate 0.5–4 $\mu\text{L}/\text{min}$; open circles, 0.75 $\mu\text{S}/\text{cm}$ and 3–7 $\mu\text{L}/\text{min}$; open triangles, 0.55 $\mu\text{S}/\text{cm}$ and flow rate 3–6 $\mu\text{L}/\text{min}$; cross, 0.55 $\mu\text{S}/\text{cm}$ at 20 °C; plus sign, 0.55 $\mu\text{S}/\text{cm}$ at 80 °C and flow rate both 3 $\mu\text{L}/\text{min}$. The solid line is a fit of all 40 °C data with a slope of 1.54. Inset: example of a measured saccharose particle size distribution; the resulting data point is marked with an arrow.

the droplet diameters are shown as a function of eq 2 with $a_d = 1$. Most data have been determined at 40 °C, except the cross, which was measured at 20 °C, and the plus sign, which was measured at 80 °C. The 40 °C temperature ensures that the particles are dry at deposition and facilitates comparison with other results in the paper, since all PVDF films have been prepared at 40 °C too. The solid line is a fit of all 40 °C data, and the slope, $a_d = 1.5$, has been used in the model to determine droplet sizes for DMF.

The calibration value, 1.5, coincides reasonably well with a general estimate for a_d of 1.1, determined by Gañán-Calvo for a range of solvents,⁶ taking into consideration that this literature value does not fit individual solvents very well and is an estimate itself. Therefore, droplet size calibration is desirable, especially if one would like to know the lifetime of a droplet accurately, since size can affect the evaporation time strongly. Temperature variation again does not appear to have a large effect on the droplet size, which is expected since flow rate and the current are the major factors in the droplet size determination. This is

convenient, because therefore droplet calibration at one single temperature can in principle be used for other (closeby) temperatures as well.

Model: Droplet Diameter as a Function of Spray Distance. In Figure 4, droplet evolution results of the model are shown; it demonstrates the transformation of the droplet evolution as a function of time (Figure 4a) into the droplet evolution as function of spray distance (Figure 4c).

The model contains three important approximations: (1) neglecting the initial speed of the droplet, (2) using a constant electric field for the calculation of the droplet velocity, and (3) averaging the droplet size and charge to calculate directly the curve in Figure 4b with eq 11. In Figure 5 the difference can be seen between the use of the approximations (solid line) and a more elaborate description (broken line): finite element calculation of the electric field, taking into account the initial velocity and the momentum of the droplet and not using the average radius and charge. As can be seen from Figure 5, the difference between the calculated distances is less than a millimeter. Furthermore, the dotted line represents the velocity and position calculated with the finite element electric field and eq 9 but without the initial velocity. The difference with the approach taking the initial velocity and momentum into account (broken line) is minimal; this indicates that under these conditions momentum is not important. The velocity of the droplet equals in both cases almost immediately the average value. Of course the larger the particle, the more the momentum will play a role; therefore, this approach will lose accuracy for droplets over 10 μm in diameter.

Size of the Film. With a stationary nozzle and substrate holder, the deposited film is circular and its radius will increase with spray distance. The relationship between the distance, s (m), and the film radius, R_{film} (m), has been determined experimentally by measuring the diameter of each deposit. For a nozzle–substrate separation from 1 to 7 cm, it was found to be

$$R_{\text{film}} = (4.7 \pm 0.2)s^2 + (0.16 \pm 0.01)s \quad (15)$$

This relationship is valid for a spray current of around 25 nA, although a current of 50 nA did not show a significant deviation from eq 15 up to 2.5 cm. At that distance, the deposit of 50 nA was dry, eliminating the need to increase the spray distance further. Nonetheless, a high spray current is expected to increase the repulsion between the droplets; therefore, relationship 15 is expected to depend on the current. Since different solvents will have different break-up patterns, droplet sizes, and droplet charge distributions, it should be expected that the deposition size relationship is different for other solvents; also the spray geometry will have an influence.

PVDF Films. A representative example of PVDF film morphologies as a function of spray distance is shown in Figure 6, where a selection of AFM images can be found of films prepared with the following conditions: flow, 3 $\mu\text{L}/\text{min}$; current, 21 nA; concentration, 0.25 wt %. At small distances (Figure 6a), most of the polymer is washed from the surface. In the second stage (Figure 6b), the deposit is somewhat drier and a surface made up of large blobs is formed. The third stage (Figure 6c–e) consists of a series of continuous films with a more or less smooth surface. Figure 6f indicates the onset of dry particles, creating a marked increase in the roughness of the film. Figure 6g is dry and so rough that it is impossible to obtain a clear image of the surface.

To compare the films, the roughness average was plotted as a function of the spray distance; in particular the continuous

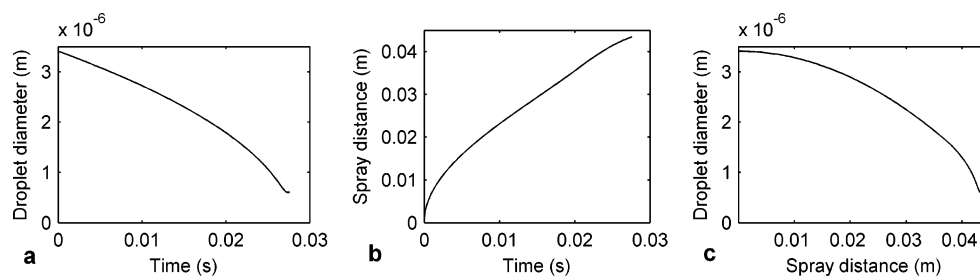


Figure 4. Droplet evolution as (a) a function of time and (c) as function of spray distance; (b) the mapping of spray distance s (eq 11) on droplet evolution time. Conditions to calculate the plots: flow, 3 $\mu\text{L}/\text{min}$; current, 21 $\mu\text{S}/\text{cm}$; concentration, 1 wt %.

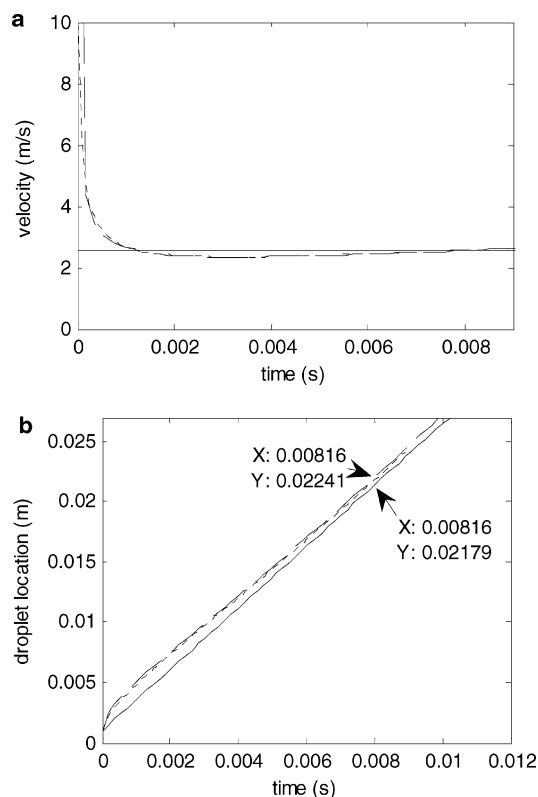


Figure 5. (a) Droplet velocity versus time. (b) Droplet location versus time: solid line, average as calculated by the model; broken line, velocity and location calculated without approximations (electric field evaluated with finite element method, initial droplet velocity calculated with eq 8 and the velocity development with eq 7 without averaging over droplet diameter and charge); dotted line, same as broken line except that the velocity is calculated with eq 9 and the initial velocity is ignored. In all cases, the entire droplet evolution has been taken into account. Conditions: flow, 3 $\mu\text{L}/\text{min}$; current, 21 $\mu\text{S}/\text{cm}$; concentration, 0.25 wt %; spray potential, 5.3 kV; spray distance set, 2.25 cm. In this graph the distance only represents the droplet location in flight, not the location of the substrate (=2.25 cm). The arrows point to the result of the model (lower) and the approach without approximations (upper).

film of Figure 6c–f is appropriately presented by the roughness. In Figure 7, the solid line without any markers represents the films of Figure 6. Following the solid line, where the letters represent the images from Figure 6, the average roughness decreases to a minimum for the continuous film and then grows while the film becomes increasingly dry. Films prepared with other droplet sizes, ranging from 1.7 to 5.0 μm , show similar patterns, albeit at different distances; the smaller the droplet, the smaller the spray distance and the more compressed the range in which the different morphologies occur. Contrary to the droplet size, the concentration does not significantly affect the spray distance of different morphologies. This is best illustrated by the spray distance for the roughness minimum of the continuous film (2.2 cm), but also the morphologies shown

in Figure 6a, b, and g can be found at the same spray distance for the other concentration series. The concentration only appears to affect the roughness average value, which is most likely not an effect of film thickness, since for each film an equal amount of polymer has been deposited.

Background Vapor Pressure. To calculate the rate of evaporation of droplets, the background pressure of the solvent within the spray (p_c , eq 4) has to be known. The pressure was determined using the spray distances that mark the onset of dry films for the flows 1.2, 3, and 6 $\mu\text{L}/\text{min}$. Flow at 1.2 $\mu\text{L}/\text{min}$ provided a dry film onset between 1.5 and 2 cm (too rough to determine a roughness average), 3 $\mu\text{L}/\text{min}$ between 4 and 5 cm, and 6 $\mu\text{L}/\text{min}$ between 7 and 8 cm. Comparing this with the droplet evolution, the possible range in background pressure was found to be 0.80–0.84 expressed as a fraction of the saturation pressure of DMF at 40 $^{\circ}\text{C}$. A dependence of this fraction on the spray distance was not found within the limits of these experiments. The background pressure p_c was therefore taken as $0.82p_{\text{DMF,saturation}}^{40^{\circ}\text{C}}$ for all calculations in this paper (although p_c is defined as the background pressure in the spray chamber, it is actually the pressure within the spray as explained in Location of the Droplet in the Theory section). The droplet evaporation is sensitive to the background pressure and the difference of the saturation fraction from 0.82 to 0.8 eliminates the difference between the calculated droplet position with the approximations of the model and with the more elaborate method. The determination of the background pressure will compensate for the error introduced by the calculation of the velocity for both approaches. Another important point is that the background vapor pressure is strongly dependent on temperature.³⁷

Viscosity. The viscosity (η) of the 5.3×10^3 g/mol PVDF solutions in DMF at 40 $^{\circ}\text{C}$ was approximated with the following sixth-order polynomial:

$$\eta = 3832200\varphi^6 - 1192200\varphi^5 + 131400\varphi^4 - 4498\varphi^3 + 84.616\varphi^2 - 0.015796\varphi + 0.000794 \quad (16)$$

with φ the volume fraction (v/v) of the polymer in the solution derived from the weight fraction and the densities of the pure compounds. The four viscosity measurements are the basis of the fit (eq 16). Literature data, scaled to the present polymer viscosity data, of a slightly smaller PVDF polymer in DMF were used to support the fit of the polynomial for concentrations below 3.5 % (v/v).³⁶ A set of 15 data points was used, resulting in a fit which properly (no oscillations) followed the course of the viscosity within the measured domain with a correlation coefficient of 1.000. For the simple reason of continuity in the model calculations, the fit has also been used for extrapolation from 16 % (v/v) up to 100 vol. %.

Results of the Model in Combination with Experiment. In Figure 8 the results are presented of the model in combination with a few experimental additions. It describes the complete

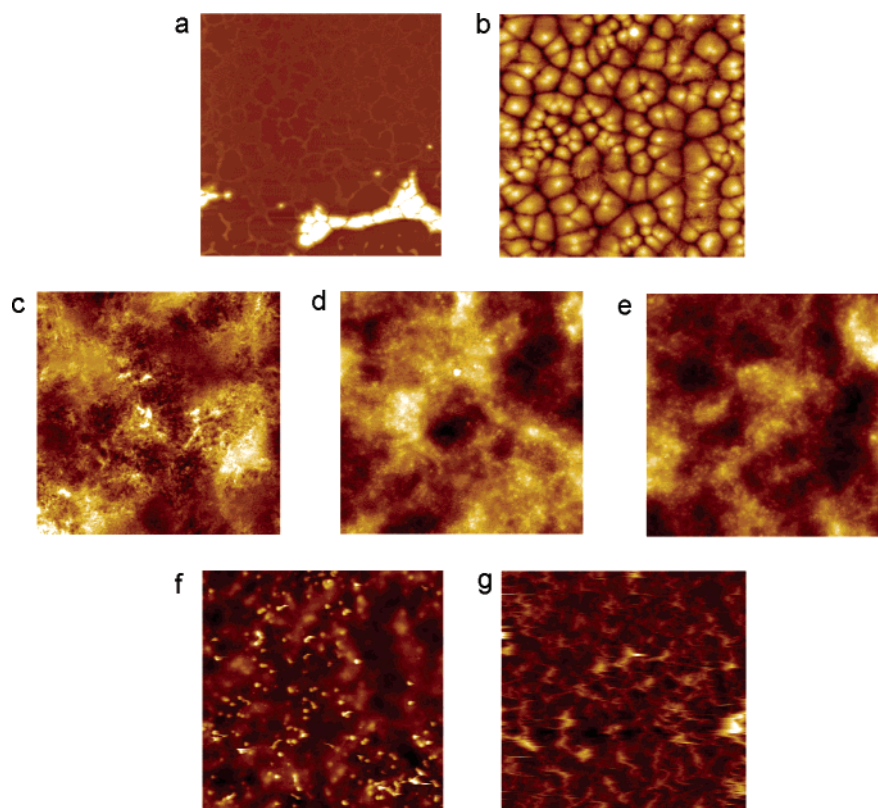


Figure 6. Example of a series of PVDF films versus spray distance. Conditions: $3 \mu\text{L}/\text{min}$; 20 nA ; $0.25 \text{ wt } \%$. Spray distances: (a) 1, (b) 1.5, (c) 2, (d) 2.5, (e) 3, (f) 4, and (g) 5 cm. Panel b has been replaced by the following: $2.5 \mu\text{L}/\text{min}$, 50 nA , and $0.25 \text{ wt } \%$ at 1 cm, because it illustrates the morphology better.

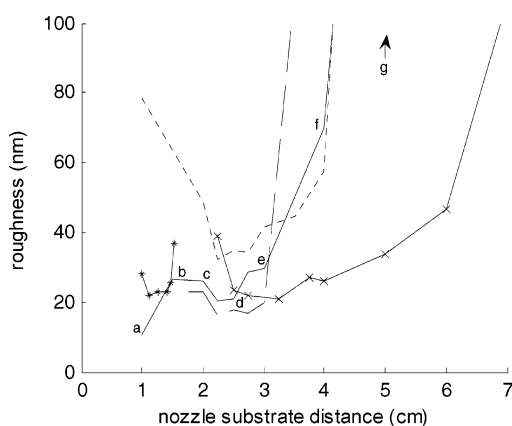


Figure 7. Roughness average of polymer films (Table 3) versus spray distance. Flow with constant concentration of $0.25 \text{ wt } \%$: solid line with asterisks (*), $1.2 \mu\text{L}/\text{min}$; solid line no marker, $3 \mu\text{L}/\text{min}$; solid line with x-marker, $6 \mu\text{L}/\text{min}$. Concentration with constant flow of $3 \mu\text{L}/\text{min}$: dotted line, $1 \text{ wt } \%$; broken line, $0.05 \text{ wt } \%$. The letters along the solid line correspond to the images in Figure 6.

state of the droplet at deposition. The droplet diameter versus spray distance (Figure 8a), the polymer concentration versus spray distance (Figure 8b), and the droplet stress at impact (Figure 8c) can all be directly calculated from the model, provided that necessary solvent constants are available (see the Appendix). The experimental quantities, size of the deposit (Figure 8d), and shear rate (Figure 8e), provide further, in part experimental, information. Once more, none of these graphs are trajectories in normal space, but a representation of a particular droplet property at the moment of deposition.

Before the relationship between the film morphologies in Figures 6 and 7 and the information from the model in Figure 8 will be discussed, it is important to pay some attention to

Figure 8 and in particular Figure 8c. In Figure 8c the stress of the droplet is given as a function of the spray distance. The stress is essentially the squared velocity of the droplet. The decrease at short spray distances is caused by the rapidly changing electric field due to the widening gap between the nozzle-ring and the substrate. This decrease levels off, when the gap becomes larger and the electric field changes more slowly. A slow rise in the velocity and stress is then caused by a size decrease of the evaporating droplet, causing the balance in eq 9 to shift slowly to higher velocities. The drop in the stress at approximately 3.7 cm is caused by a decrease in charge due to the Rayleigh limit. Since the droplet will continue to evaporate from here on, the charge on the droplet will decrease not to exceed the Rayleigh charge limit; therefore, the electric force will decrease. Since this plot presents the state of the droplets creating the films in Figure 6 (the solid line in Figure 7), it can be seen that only the last two, rough, films may be affected by discharge and solvent loss due to the Rayleigh limit as discussed in the Introduction and the Theory sections. The more interesting films on the other hand are prepared with droplets that impinge before the Rayleigh limit has been reached.

5. Discussion

PVDF films show four distinct morphologies with electro-spray deposition as a function of flow rate, conductivity, and concentration: (1) a liquid, which in large part runs from the substrate during the spray, hereafter, “liquid” morphology; (2) globulelike deposit, hereafter, “blobs” morphology; (3) continuous film, which appears to be the smoothest of the four morphologies, hereafter “continuous” morphology; and the latter is followed by a gradual transition to (4) a rough film consisting of dry particles, hereafter, “dry” morphology. The causes for the liquid and dry morphologies are clear; they result from an

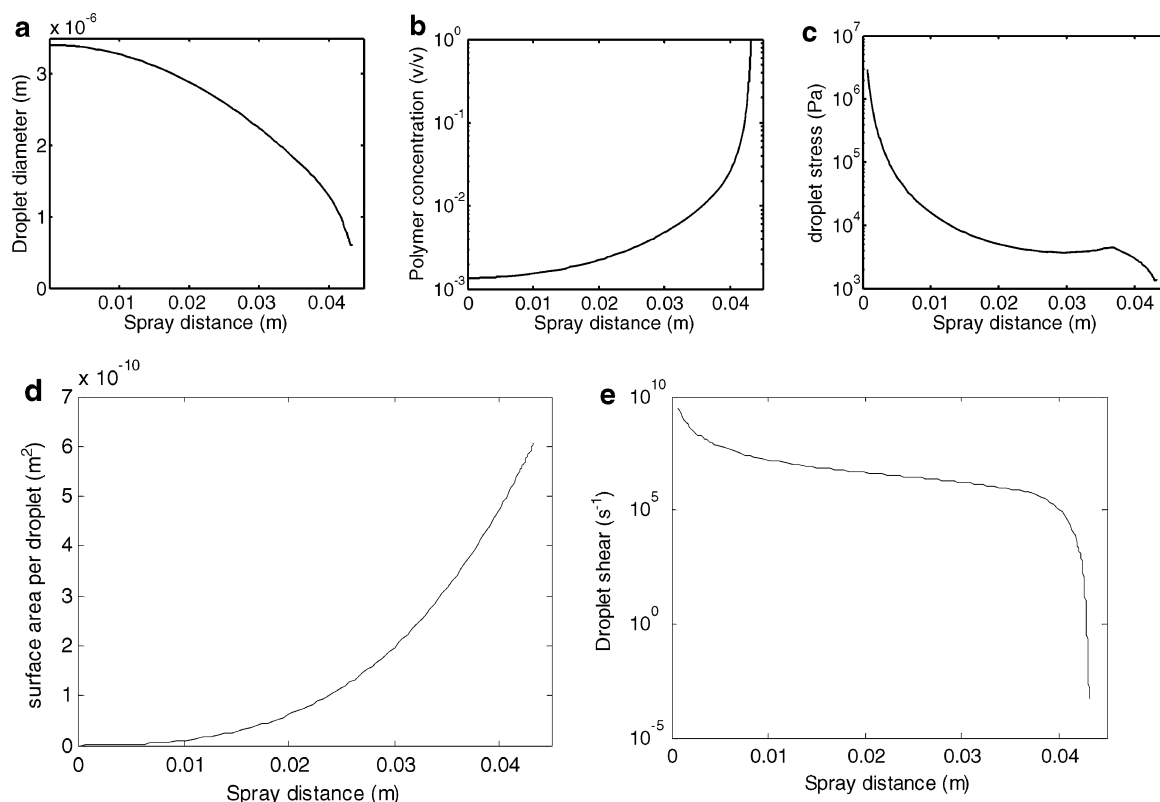


Figure 8. Results obtained with the model versus spray distance: (a) droplet diameter; (b) polymer concentration; (c) shear stress on droplet (eq 12); (d) surface area per droplet per second (eqs 15 and 2 and input flow rate); (e) shear rate (eqs 13 and 16). Conditions for this example are 3 $\mu\text{L}/\text{min}$, 21 nA, and 0.25 wt %.

excess of and a total lack of solvent, respectively. Continuous morphology exists, since polymer solution is expected to flow moderately and to form more or less interconnected networks. This has been discussed in a previous paper,¹⁶ where viscosity was mentioned as the main control factor of the smoother continuous film. The droplet size was mentioned as another important factor determining film morphology.

The role of the viscosity and the droplet size can be studied with the help of Figure 7. If viscosity, which is proportional to the concentration (eq 16), increases, the roughness increases too, but the spray distance of a particular morphology does not change. Apparently, the viscosity (or concentration) does not determine the type of morphology, but merely modifies the existing morphology; it affects in particular the continuous morphology and has less or no effect on the blob and liquid morphology. On the other hand, the droplet size has a significant influence on the spray distance of a certain morphology. In first instance, it would be appealing to correlate this to the concentration, for smaller droplets evaporate faster and therefore will reach a particular concentration and viscosity faster, but this is ruled out by the observations discussed above.

The explanation can be found in Figure 9, where the volume of the impinging droplet is plotted against its available surface on the substrate. The available surface per droplet is calculated with the initial droplet size (eq 2) and the flow to determine the number of droplets generated per second, in combination with the size of the deposit (eq 15) as a function of the spray distance. The markers in the graph represent films, sprayed at set distances, and therefore they will not always perfectly coincide with the locations of the mapped morphologies. The occurrences of the different morphologies in Figure 9 follow reasonably straight lines within the domain studied in the paper.

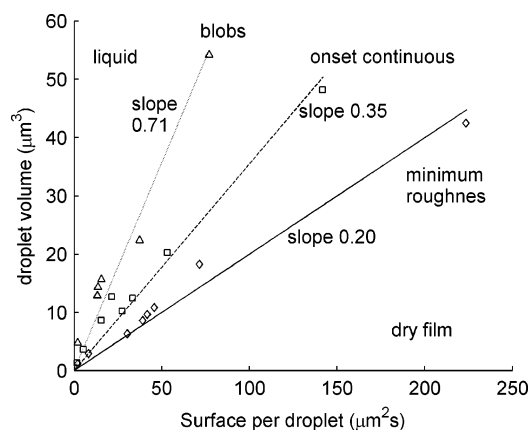


Figure 9. Droplet volume versus the available surface per droplet per second: triangles, blobs morphology; squares, onset of continuous morphology; diamonds, minimum roughness of continuous morphology. The lines are fits of the respective morphologies, and the slopes have the unit $\mu\text{m}/\text{s}$, representing growth of solution per second on the substrate.

These lines are linear fits of the data and can be considered growth rates of the respective morphologies with the unit $\mu\text{m}/\text{s}$.

Growth rate apparently determines which morphology to expect, but other factors must have an influence on the properties of the films. At growth rates higher than 0.7 $\mu\text{m}/\text{s}$ liquid runs from the substrate. It indicates that the deposit does not have enough time to dry and builds up, causing droplets to coalesce. Even though the solution contains polymer, its concentration increases only slowly with evaporation (cf. Figure 8b); therefore, the viscosity will not be much higher than 10 times the solvent value, which means that the solution will flow without hindrance.

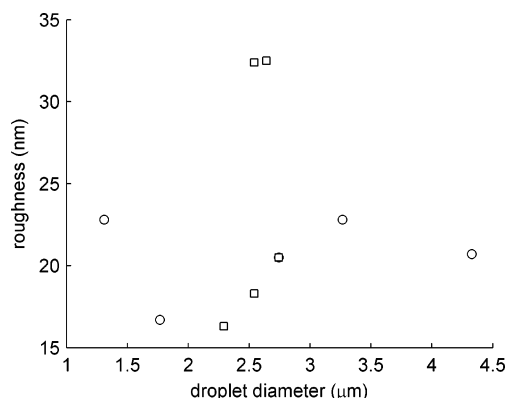


Figure 10. Minimum roughness average of all film series (Table 3) versus the droplet diameter at deposition: open squares, concentration series; open circles, droplet size series.

In the case of the blobs morphology the growth rate has diminished to such an extent that droplet coalescence does not occur anymore. Instead, the bloblike structure could be explained as the result of single droplets that have enough time to dry to leave a polymer particle behind. This cannot be the complete explanation; otherwise, the morphology at even lower growth rate should consist of drier particles; instead it is a smooth continuous film. Therefore, the blobs morphology probably forms with single droplets depositing on the surface, leaving a wet polymer particle behind. This wet polymer particle becomes part of another droplet that deposits afterward, possibly partly dissolving again. This can be the explanation of the groovelike patterns, which divide the blobs (Figure 6b) and resemble droplet structures. The specific shape of the blobs is probably determined by the surface energy interactions between the solution and the substrate.

The slope of $0.35 \mu\text{m/s}$ in Figure 9 indicates the onset of continuous film. Films made with a growth rate of $0.20 \mu\text{m/s}$ pass through the lowest roughness averages for this combination of polymer, solvent, temperature, and substrate. First, the formation of the smoothest continuous film will be discussed. After that, we will discuss the onset of continuous film.

Smooth continuous film is formed by droplets impinging on the surface with a relatively low viscosity and a capability to flow, as was already concluded above. With the lower growth rate of $0.20 \mu\text{m/s}$, the droplets have sufficient time to dry and are not strongly affected by the next impinging droplet; however, the polymer film still contains enough solvent to mix with the next droplet. Moreover, impinging droplets completely deform in the case of the smoothest film. This can be seen in Figure 10, where the roughness average of the smoothest films is plotted versus the diameter of the impinging droplet. No clear correlation with the roughness average can be found, indicating that the droplet size does not play an important role in the determination of the roughness average. This is a strong indication that the droplet completely deforms, leaving no trace of its size. The surface energy difference in this regime can be eliminated as an important film formation factor, since most of the film will deposit on top of other polymer film already deposited, which means that there is no change in the surface energy during deposition. The surface energy difference between the substrate and the first layer of polymer may play a role however, to which extent still needs to be investigated.

With the surface energy and the droplet size eliminated, the only remaining parameters that could influence film formation are the viscosity (concentration) and the velocity of the droplets. A plot of the minimum roughness average versus the viscosity

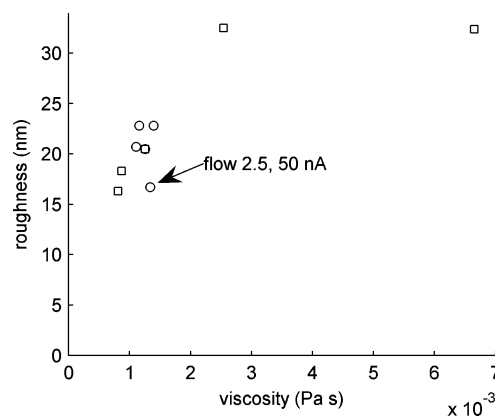


Figure 11. Minimum roughness average of all film series (Table 3) versus viscosity (eq 16) at deposition: open squares, concentration series; open circles, droplet size series. The roughness of $2.5 \mu\text{L/min}$, 50 nA is low in comparison to its viscosity.

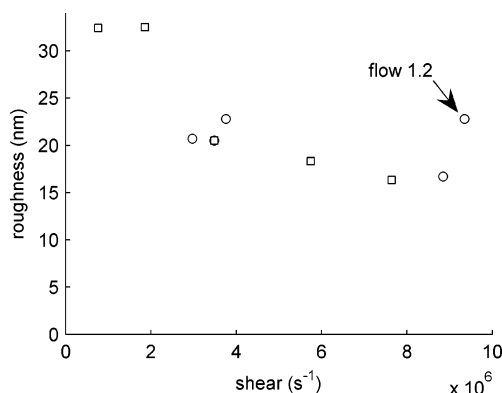


Figure 12. Minimum roughness average of all film series (Table 3) versus shear rate (eq 13) at deposition: open squares, concentration series; open circles, droplet size series. The roughness of $1.2 \mu\text{L/min}$ has a high roughness in relation to its shear rate.

can be found in Figure 11. There is a relationship of the viscosity with the roughness average; a decrease in viscosity provides smoother film. Therefore, droplet flow is also expected to be an important factor for film smoothness. Plotting the minimum roughness versus the flow of the droplets in the form of the shear rate, the roughness decreases with an increasing shear rate (Figure 12). The viscosity outlier with flow $2.5 \mu\text{L/min}$ and 50 nA in Figure 11 follows the relationship with the shear rate, because its velocity and therefore its shear stress is much higher due to the high charge on its droplets. Only the smallest droplet, $1.2 \mu\text{L/min}$, does not follow the relationship with the shear rate; the reason is unclear.

Since the shear rate shows a convincing relationship with the minimum roughness, it is expected that such a relationship also exists for continuous films with even lower growth rates. This can be seen in Figure 13, where roughness average values are plotted of various continuous films. The relationship between the roughness average and the shear rate can be reasonably well described with a simple power law relationship, $900\gamma^{-0.25}$, which matches the roughness average of films from different initial conditions simultaneously. That the roughness average is described by a simple power law is additional evidence that the shear rate is the main factor determining the roughness of the continuous film (not only of the roughness minimum).

From Figure 13 follows that an increase in shear rate means a decrease in roughness average. Films with a growth rate of $0.35 \mu\text{m/s}$ (Figure 9) are continuous but have a higher roughness average. The reason behind this is that these films are in an

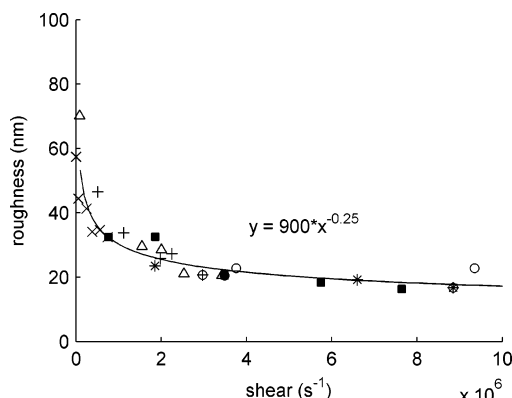


Figure 13. Roughness average of various films with growth rates ranging from 0.20 to $\sim 0 \mu\text{m/s}$ versus shear rate: open squares, roughness minima of the concentration series; open circles, droplet size series; asterisk, $2.5 \mu\text{L/min}$ series; triangles, $3 \mu\text{L/min}$ series with 0.25 wt %; crosses, 1 wt % series; plus sign, $6 \mu\text{L/min}$ series. The line is the power law relationship of all the presented data combined.

intermediate region, where the growth rate is too high to allow for sufficient drying of the deposited droplet before the next droplet impinges. Therefore, the film on the substrate is wetter, which increases its tendency to deform under impact, and it may also increase the effect of surface tension interactions with the substrate. In addition, there may be a limit to the increase of the shear rate, since too high shear rates can cause the droplet to flow up from the surface, which will increase the roughness average. However, the latter effect is not expected to be the explanation for the roughness of the onset of continuous film, since many of the onset films have a lower shear rate than some of the smoothest films. Flow 1.2 in Figure 12 may be an indication that the optimum shear rate has been reached, but the fact that the minimum smoothness spray distance for flow 1.2 is difficult to determine, due to the narrow interval in the spray distance (Figure 7), only shows that more research is needed to determine the true maximum of the shear rate. Therefore, a combination of the shear rate, film deformation under droplet impact, and surface tension is most likely controlling the intermediate region. One could argue that in the case of the blobs morphology the surface tension has the upper hand, whereas in the onset of the continuous film the main factors determining the film morphology are the droplet shear rate and the film deformation caused by the droplet impact. More research will be needed to define the role of the different factors more precisely.

Although the experimental results in this paper concern a polymer, the understanding of morphologies prepared with electrospray deposition in terms of growth rates can be applied on a more general basis. Since dry particles create in general loose, rough films, unless specific properties of the particles allow otherwise, electrospray is most controllable if solvent is still present at deposition. In the case of polymers, the regime where the shear rate is the sole parameter determining the film roughness is probably large in comparison with solutions with a lower viscosity, but that does not have to mean that the regime is not present in the case of low-viscosity compounds. In less viscous solutions, the continuous film growth rates will be much lower than for PVDF, meaning that more solvent has to evaporate to make the film resistant against solvent impact or surface tension effects. To realize this, one can raise the vapor pressure of the solvent indirectly by raising the temperature. This is exactly what happens in spray pyrolysis of inorganic compounds, where the temperature of the substrate is brought close to or slightly over the boiling point of the solvent.^{13,19} An

advantage of heating the substrate is that one can control the vapor pressure of the solvent in the droplet and on the surface separately, which is especially useful if there is a chance of precipitation of the solute in the droplet.¹³ In the case of organic compounds, however, other ways may have to be found to reach the same result (such as the use of viscosity).

Furthermore, when the substrate temperature for electrospray pyrolysis is lowered, structures such as cracks¹³ or holes¹⁹ often form, which are both examples of a higher growth rate, in this case induced by the temperature. The films crack or show holes due to the evaporation of residual solvent,^{13,19} which is an indication that electrospray deposition is now in the intermediate regime, coping with effects of the solvent. Because these examples concern inorganic films, other parameters might be more important than in the case of polymers or organic compounds in general. The essence is, however, that with the model presented in this paper, growth rate will be defined by a limited number of spray variables. The growth rate is related to the film morphologies, which will also depend on a few important parameters, such as shear rate, deformation under impact, and surface tension. With the use of growth rate as the key to film morphologies, a general control of film morphologies with electrospray deposition should become in reach.

6. Conclusions

Prediction of the current, eq 1, facilitates the planning of an experiment although the proportionality constant a_I needs to be determined in advance. The temperature effect of the current is small, and the use of the conductivity determined at 20°C appears to be sufficient for application in the model, at least in the range from 20 to 80°C .

Calibration of eq 2 is necessary, if the size of the droplet is important. It is recommended for the accuracy of the model, but there are literature values which can be used too. An incorrect droplet size may in part be corrected by the determination of the background solvent vapor pressure in the chamber. In its present form, the model does not incorporate compensating factors for the evaporation of large or extremely small droplets. Its droplet diameter validity range is roughly $1\text{--}10 \mu\text{m}$.

The model provides diameter, concentration, and shear stress of the droplet as a function of time. With the assumptions of a constant electric field, average values for the droplet diameter and droplet charge, and negligible droplet momentum, time can be directly related to the spray distance, s . With additional experimental data, such as the solution viscosity and the diameter of the film deposit with distance, a complete picture of the state of the droplet at impact can be obtained.

Given the solvent, the solute, and a defined spray geometry, the model reduces the electrospray control variables to flow rate, conductivity of the solution, solute concentration, the temperature, and the substrate parameters. Film morphology can be expressed in terms of a few main factors including growth rate, shear rate, and surface energy. Most of the other parameters, such as viscosity, temperature, and vapor pressure, have an influence on the morphology, but they act through one of the three main factors.

Growth rate acts as the indicator of the morphology. If the growth rate is low enough, the roughness average of PVDF film is completely determined by the shear rate of the impinging droplet and the relationship between the roughness and the shear rate can be described by simple power law behavior. Smooth continuous film needs a growth rate low enough to provide time for the deposit to dry and a high shear rate for the film to spread over the surface. At higher growth rates, the combination of

shear rate and interfacial energies can create interesting and complicated morphologies. An example of such a morphology is a bloblike structure formed by PVDF under specific conditions.

These results may be applied to electrospray deposition in general. That is not to say that this analysis explains all deposition phenomena directly, but it provides a simple framework, which captures the main aspects of film formation with electrospray deposition.

Acknowledgment. We thank Prof. Takigawa and Dr. Urayama of Kyoto University for their help with the viscosity measurements. I.B.R. thanks Prof. D. Bedeaux for discussing some theoretical implications of the experimental results. This work was supported by the Integrated Industry Academia Partnership (IIAP), Kyoto University International Innovation Center.

Appendix

Determination of a Flat Velocity Profile. The presence of a flat velocity profile can be determined with⁷

$$\delta = \left(\frac{\sigma^3 \epsilon_0^2}{\eta^3 K^2 Q} \right)^{1/3} \quad (\text{A1})$$

with σ surface tension, ϵ_0 dielectric constant of vacuum, η viscosity of the solution, K conductivity of the solution, and Q flow rate.

If the dimensionless parameter $\delta < 1$, the velocity profile is flat and eq 1 can be used. If $\delta > 1$, the viscosity is too low to generate a flat velocity profile and the following equation can be used to calculate the current:⁷

$$I \sim (\sigma^3 \epsilon_0 K Q / \rho)^{1/4} \quad (\text{A2})$$

with ρ the density of the solution (solvent). Also in this case a proportionality constant will have to be determined; a possible value is given in ref 7. Nonetheless eq 1 appears to be fairly robust and is applicable even though the data in this paper have a value for δ which is higher than 1 (1–5).

Motionless Droplet Approximation for the Droplet Evaporation. The correction factor f in eq 4 is equal to $f = 0.5Sh$, with Sh the Sherwood number:^{31,38,39}

$$Sh = 2(1 + 0.3Re^{1/2}Sc^{1/3}) \quad (\text{A3})$$

with Re the Reynolds number and Sc the Schmidt number. The Reynolds number in the case of a moving droplet is

$$Re = \frac{\rho U_0 d}{\mu} \quad (\text{A4})$$

with ρ the density of the surrounding medium, U_0 the velocity of the droplet relative to the surrounding medium, d the diameter of the droplet, and μ the dynamic viscosity of the surrounding medium.

The Schmidt number is

$$Sc = \frac{\mu}{\rho D} \quad (\text{A5})$$

with D the diffusion coefficient of the evaporating compound.

In the present case, droplets have a diameter in the order of 3×10^{-6} m and a velocity in the order of 3 m/s (Figures 4 and 5). Using the constants given below, eq A3 becomes 2.18. This

means that the error of taking $Sh = 2$ is in the order of 10%. It should also be kept in mind that the air in the spray is most likely not stagnant but will move along with the spray; therefore Re is lower than assumed in this calculation, allowing for the approximation $f = 1$ in eq 4. For larger droplets, especially those over 10 μm , the approximation $f = 1$ will not hold anymore and eq A3 will have to be used.

The heat exchange of the droplet with the surrounding medium obeys a similar relationship as presented for the mass exchange. More information can be found in refs 31, 38, and 39.

Constants Used in the Model Calculations.^{40,41} Heat-transfer coefficient of air, 2.51×10^{-2} J/(m s K); viscosity of nitrogen gas, 1.7×10^{-5} Pa s; working temperature, 313 K (40 °C); potential of the ring, 3000 V; potential nozzle, see Table 2.

DMF. Density, 950 kg/m³; molar weight, 0.07309 kg/mol; heat of evaporation, 4.69×10^4 J/mol; heat capacity, 2060 J/(kg K); surface tension, 0.0371 N/m; Antoine coefficients for vapor pressure, $A = 6.05286$, $B = 1400.86$, and $C = -76.716$; diffusion of DMF molecule in air, 1.2×10^{-5} m²/s (estimate by lack of literature data, $1/2 \times$ oxygen diffusion). The partial pressure of DMF in the chamber was determined from experiment as $0.82p_{\text{DMF,saturation}}^{40^\circ\text{C}}$ (the saturation pressure of DMF at 40 °C).

PVDF. Density, 1750 kg/m³; molar weight, 540 kg/mol.

The calibration constant $a_d = 1.5368$ determined with sucrose as described in the paper for eq 2. Literature “calibration constant” can be found in refs 6 and 7.

Supporting Information Available: Program code of the droplet evaporation model as described in Theory written in Matlab Version 7.1.0.246 (R14). This material is available free of charge via the Internet at <http://pubs.acs.org>.

References and Notes

- (1) Fenn, J. B. *Angew. Chem., Int. Ed.* **2003**, *42*, 3871.
- (2) Whitehouse, C. M.; Dreyer, R. N.; Yamashita, M.; Fenn, J. B. *Anal. Chem.* **1985**, *57*, 675.
- (3) Chen, D.-R.; Pui, D. Y. H.; Kaufman, S. L. *J. Aerosol Sci.* **1995**, *26*, 963.
- (4) Cloupeau, M. *J. Aerosol Sci.* **1994**, *25*, 1143.
- (5) Cloupeau, M.; Prunet-Foch, B. *J. Electrostat.* **1989**, *22*, 135.
- (6) Ganán-Calvo, A. M. *Phys. Rev. Lett.* **1997**, *79*, 217.
- (7) Ganán-Calvo, A. M.; Davila, J.; Barrero, A. *J. Aerosol Sci.* **1997**, *28*, 249.
- (8) Hartman, R. P. A.; Brunner, D. J.; Camelot, D. M. A.; Marijnissen, J. C. M.; Scarlett, B. *J. Aerosol Sci.* **1999**, *30*, 823.
- (9) Hartman, R. P. A.; Brunner, D. J.; Camelot, D. M. A.; Marijnissen, J. C. M.; Scarlett, B. *J. Aerosol Sci.* **2000**, *31*, 65.
- (10) Xie, J.; Marijnissen, J. C. M.; Wang, C.-H. *Biomaterials* **2006**, *27*, 3321.
- (11) Reneker, D. H.; Hou, H. *Electrospinning. Encyclopedia of Biomaterials and Biomedical Engineering*; 2004; Vol. 1, p 543.
- (12) Chen, C. H.; Emond, M. H. J.; Kelder, E. M.; Meester, B.; Schoonman, J. *J. Aerosol Sci.* **1999**, *30*, 959.
- (13) Wilhelm, O.; Pratsinis, S. E.; Perednis, D.; Gauckler, L. J. *Thin Solid Films* **2005**, *479*, 121.
- (14) Fujitsuka, N.; Sakata, J.; Miyachi, Y.; Mizuno, K.; Ohtsuka, K.; Taga, Y.; Tabata, O. *Sens. Actuators, A* **1998**, *A66*, 237.
- (15) Hoyer, B.; Sorensen, G.; Jensen, N.; Nielsen, D. B.; Larsen, B. *Anal. Chem.* **1996**, *68*, 3840.
- (16) Rietveld, I. B.; Kobayashi, K.; Yamada, H.; Matsushige, K. *J. Colloid Interface Sci.* **2006**, *298*, 639.
- (17) Sakata, J.; Mochizuki, M. *Thin Solid Films* **1991**, *195*, 175.
- (18) Berkland, C.; Pack, D. W.; Kim, K. *Biomaterials* **2004**, *25*, 5649.
- (19) Leeuwenburgh, S. C. G.; Heine, M. C.; Wolke, J. G. C.; Pratsinis, S. E.; Schoonman, J.; Jansen, J. A. *Thin Solid Films* **2006**, *503*, 69.
- (20) Morota, K.; Matsumoto, H.; Mizukoshi, T.; Konosu, Y.; Minagawa, M.; Tanioka, A.; Yamagata, Y.; Inoue, K. *J. Colloid Interface Sci.* **2004**, *279*, 484.

- (21) Saf, R.; Goriup, M.; Steindl, T.; Hamedinger, T. E.; Sandholzer, D.; Hayn, G. *Nat. Mater.* **2004**, *3*, 323.
- (22) Cloupeau, M.; Prunet-Foch, B. *J. Aerosol Sci.* **1994**, *25*, 1021.
- (23) Barrero, A.; Ganan-Calvo, A. M.; Davila, J.; Palacios, A.; Gomez-Gonzalez, E. *J. Electrostat.* **1999**, *47*, 13.
- (24) Ganan-Calvo, A. M. *J. Fluid Mech.* **1997**, *335*, 165.
- (25) Smith, K. L.; Alexander, M. S.; Stark, J. P. W. *J. Appl. Phys.* **2006**, *99*, 064909/1.
- (26) Larsen, G.; Spretz, R.; Velarde-Ortiz, R. *Adv. Mater.* **2004**, *16*, 166.
- (27) Hinds, W. C. *Aerosol Technology, Properties, Behavior, and Measurement of Airborne Particles*, 2nd ed.; John Wiley & Sons: New York, 1998.
- (28) *Electrospray Ionization Mass Spectrometry*; Cole, R. B., Ed.; John Wiley & Sons: New York, 1997.
- (29) Ganan-Calvo, A. M.; Lasheras, J. C.; Davila, J.; Barrero, A. *J. Aerosol Sci.* **1994**, *25*, 1121.
- (30) Freund, L. B.; Suresh, S. *Thin Film Materials: Stress, Defect Formation and Surface Evolution*; Cambridge University Press: Cambridge, U.K., 2003.
- (31) Wilhelm, O.; Madler, L.; Pratsinis, S. E. *J. Aerosol Sci.* **2003**, *34*, 815.
- (32) Xiong, Y.; Kostas, T. T. *J. Aerosol Sci.* **1993**, *24*, 893.
- (33) Clift, R.; Grace, J. R.; Weber, M. E. *Bubbles, Drops, and Particles*; Academic Press: New York, 1978.
- (34) Smedley, S. I. *The Interpretation of Ionic Conductivity in Liquids*; Plenum Press: New York, 1980.
- (35) Barabási, A.-L.; Stanley, H. E. *Fractal Concepts in Surface Growth*; Cambridge University Press: Cambridge, U.K., 1995.
- (36) Ambrosone, L.; Della Volpe, C.; Guarino, G.; Sartorio, R.; Vitagliano, V. *J. Mol. Liq.* **1991**, *50*, 187.
- (37) Wilhelm, O.; Madler, L. *Atomization Sprays* **2006**, *16*, 83.
- (38) Bird, R. B.; Stewart, W. E.; Lightfoot, E. N. *Transport Phenomena*, 2nd ed.; John Wiley & Sons: New York, 2002.
- (39) Fuchs, N. A. *Evaporation and Droplet Growth in Gaseous Media*; Pergamon Press: London, 1959.
- (40) *Handbook of Chemistry and Physics*, 86th ed.; Lide, D. R., Ed.; CRC Press: Boca Raton, FL, 2005.
- (41) *Landolt-Börnstein*; Martienssen, W., Ed.; Springer-Verlag: Berlin, 2000.